









## Vibrational properties of SrVO<sub>2</sub>H with large spin-phonon coupling

Rasmus Lavén <sup>1</sup>, Pedro Ivo R. Moraes <sup>2</sup>, Michael Sannemo Targama <sup>3</sup>, Maths Karlsson <sup>1</sup>, Alexandre A. Leitão,<sup>2</sup> Paulo H. B. Brant Carvalho <sup>3</sup>, Stewart F. Parker <sup>4</sup>, Ulrich Häussermann <sup>3,\*</sup> and Olga Yu. Vekilova <sup>3</sup>

<sup>1</sup>Department of Chemistry and Chemical Engineering, Chalmers University of Technology, SE-412 96 Göteborg, Sweden

<sup>2</sup>Department of Chemistry, Federal University of Juiz de Fora, Juiz de Fora-MG, 36036-900, Brazil

<sup>3</sup>Department of Materials and Environmental Chemistry, Stockholm University, SE-10691, Sweden

<sup>4</sup>ISIS Neutron and Muon Source, STFC Rutherford Appleton Laboratory, Oxfordshire OX11 0QX, United Kingdom



(Received 10 November 2021; accepted 27 January 2022; published 28 February 2022)

The antiferromagnetic transition metal oxyhydride SrVO<sub>2</sub>H is distinguished by its stoichiometric composition and an ordered arrangement of H atoms. The tetragonal structure is related to the cubic perovskite and consists of alternating layers of VO<sub>2</sub> and SrH. *d*<sup>2</sup> V(III) attains a sixfold coordination by four O and two H atoms. The latter are arranged in a trans fashion, which produces H–V–H chains along the tetragonal axis. Here, we investigate the vibrational properties of SrVO<sub>2</sub>H by inelastic neutron scattering and infrared spectroscopy combined with phonon calculations based on density functional theory. The H-based vibrational modes divide into a degenerate bending motion perpendicular to the H–V–H chain direction and a highly dispersed stretching motion along the H–V–H chain direction. The bending motion, with a vibrational frequency of approximately 800 cm<sup>−1</sup>, is split into two components separated by about 50 cm<sup>−1</sup>, owing to the doubled unit cell from the antiferromagnetic structure. Interestingly, spin-phonon coupling stiffens the H-based modes by 50–100 cm<sup>−1</sup> although superexchange coupling via H is very small. Frequency shifts of the same order of magnitude also occur for V–O modes. It is inferred that SrVO<sub>2</sub>H displays the hitherto largest recognized coupling between magnetism and phonons in a material.

DOI: [10.1103/PhysRevMaterials.6.024409](https://doi.org/10.1103/PhysRevMaterials.6.024409)

### I. INTRODUCTION

Transition metal (T) oxyhydrides are a small but steadily growing family of mixed anion materials which are based on the rather unlike anions O<sup>2−</sup> and H<sup>−</sup>. They are of considerable current interest due to unique properties introduced by the hydride ion, affecting magnetism, electron, and ion transport as well as catalytic activity [1]. T oxyhydrides are obtained by hydride reduction of perovskite and Ruddlesden-Popper phase oxide precursors (according to, e.g., SrVO<sub>3</sub> + CaH<sub>2</sub> → SrVO<sub>2</sub>H + CaO + 1/2 H<sub>2</sub> [2]) or directly from mixtures of binary oxides and hydrides using high-pressure synthesis (according to, e.g., SrH<sub>2</sub> + SrO + Cr<sub>2</sub>O<sub>3</sub> → 2 SrCrO<sub>2</sub>H [3]). The simplest systems derive directly from the simple cubic perovskite structure, yet—depending on the kind of T and H content and distribution—different scenarios are encountered. To illustrate the versatility of T oxyhydrides, both BaTiO<sub>3−x</sub>H<sub>x</sub> (with *x* up to 0.6) [4,5] and SrCrO<sub>2</sub>H [3] are afforded with an average cubic perovskite structure in which O<sup>2−</sup> and H<sup>−</sup> display a perfect solid solution behavior

[Fig. 1(a)]. In contrast, for SrVO<sub>2</sub>H, which has the same stoichiometry as SrCrO<sub>2</sub>H, the H atoms appear perfectly ordered in a tetragonal structure, Fig. 1(b) [2]. BaTiO<sub>3−x</sub>H<sub>x</sub> with Ti in a mixed IV/III oxidation state is paramagnetic (above the lowest temperature measured, 5 K [4]). SrCrO<sub>2</sub>H containing Cr(III) *d*<sup>3</sup> species (*S* = 3/2) and SrVO<sub>2</sub>H containing V(III) *d*<sup>2</sup> species are both antiferromagnets where strong couplings are maintained above room temperature. The Néel temperature *T*<sub>N</sub> of SrCrO<sub>2</sub>H is 380 K [3] and >430 K for SrVO<sub>2</sub>H [2,6]. A G-type antiferromagnetic (AFM) structure with a ten-atom unit cell is realized for both SrCrO<sub>2</sub>H and SrVO<sub>2</sub>H [2,3] and is depicted (for H<sup>−</sup> ordered SrVO<sub>2</sub>H) in Fig. 1(c).

The bonding situation of H in T oxyhydrides is still not well explored. Naturally, the introduction of H in ATO<sub>3</sub> oxides (A=alkali, alkaline earth, rare earth metal) leads to disruption of the three-dimensional T–O π bonding pattern since T–H interactions are exclusively σ type in nature. T–H bonding appears comparatively weak and creates an inherent lability for the hydride ion. This is especially known for BaTiO<sub>3−x</sub>H<sub>x</sub>, for which above 400 °C the exchange of H by deuterium (D) and N in the presence of D<sub>2</sub> and N<sub>2</sub>, respectively, has been observed [4,7,8]. In the case of stoichiometric and ordered SrVO<sub>2</sub>H, with H atoms arranged exclusively in the trans location of the octahedral environment around V(III), π interactions are effectively blocked along the *c* direction, rendering this material as quasi-2D. This is, for example, reflected in the superexchange interactions, which are strong via the oxide ligands and small, although not negligible, via the H ligands [9,10]. An interesting conclusion was derived

\*ulrich.haussermann@mmk.su.se

Published by the American Physical Society under the terms of the Creative Commons Attribution 4.0 International license. Further distribution of this work must maintain attribution to the author(s) and the published article's title, journal citation, and DOI. Funded by Bibsam.

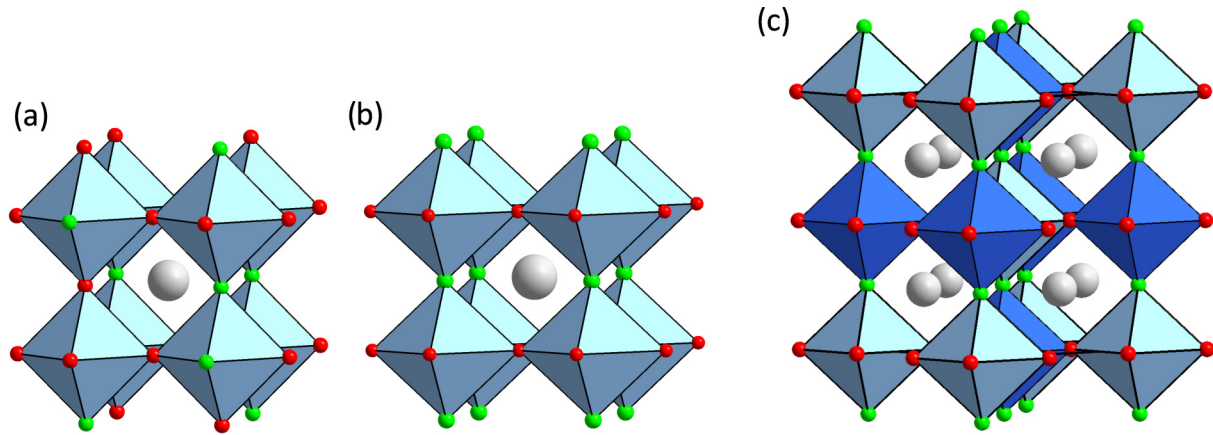


FIG. 1. Crystal structures of cubic SrCrO<sub>2</sub>H (a) with randomly distributed H ions and of H-ordered primitive tetragonal SrVO<sub>2</sub>H (five-atom structure) (b). (c) Tetragonal body-centered AFM structure of SrVO<sub>2</sub>H (ten-atom structure). Light and dark blue octahedra enclose V ions with spin-up and -down orientations, respectively. Small green and red circles denote H and O ions, respectively. Large grey circles denote Sr ions.

in the theoretical study by Liu *et al.* [10], namely, that the introduction of H actually enhances the V–O superexchange coupling through more delocalized *d* orbitals.

To shed more light into the nature of T–H interactions in T oxyhydrides, we have performed a vibrational property study of SrVO<sub>2</sub>H. The techniques used are inelastic neutron scattering (INS), infrared (IR) spectroscopy, and phonon calculations based on density functional theory (DFT). Of relevance here, some of us recently reported on a combined INS and DFT study of the similar oxyhydride material BaTiO<sub>3–x</sub>H<sub>x</sub> [11,12]. The results from that study showed that the H vibrations, manifested as Ti–H bending and stretching modes at around 900 and 1030 cm<sup>–1</sup>, respectively, are localized in nature [Fig. 2(a)]. In addition, the extra electrons introduced with Ti reduction conform to a delocalized electronic band state of the material, as opposed to bound electron polarons [11,12]. At the same time, the relatively low vibrational frequencies confirmed a rather loosely bonded H

in the material. Ordered SrVO<sub>2</sub>H represents a rather different scenario as the linear . . . –H–V–H–V–H–. . . chains along the tetragonal directions would suggest dispersed phonons [Fig. 2(b)]. A further interesting issue is the influence of magnetism on phonons/vibrational properties. Indeed, we show that the AFM spin-phonon interaction introduces large frequency shifts, particularly for H-dominated modes, even though the interlayer coupling is very weak.

## II. METHODS

### A. Material synthesis

SrVO<sub>2</sub>H powder was synthesized by hydride reduction of the perovskite SrVO<sub>3</sub> with CaH<sub>2</sub>. The procedure essentially followed the original report by Romero *et al.* [2] with some slight modifications. 5 g (26.8 mmol) of SrVO<sub>3</sub>, which was prepared from SrCO<sub>3</sub> (ABCR, 99.9% purity) and V<sub>2</sub>O<sub>5</sub> (Sigma Aldrich, 99.6% trace metal basis) according to the

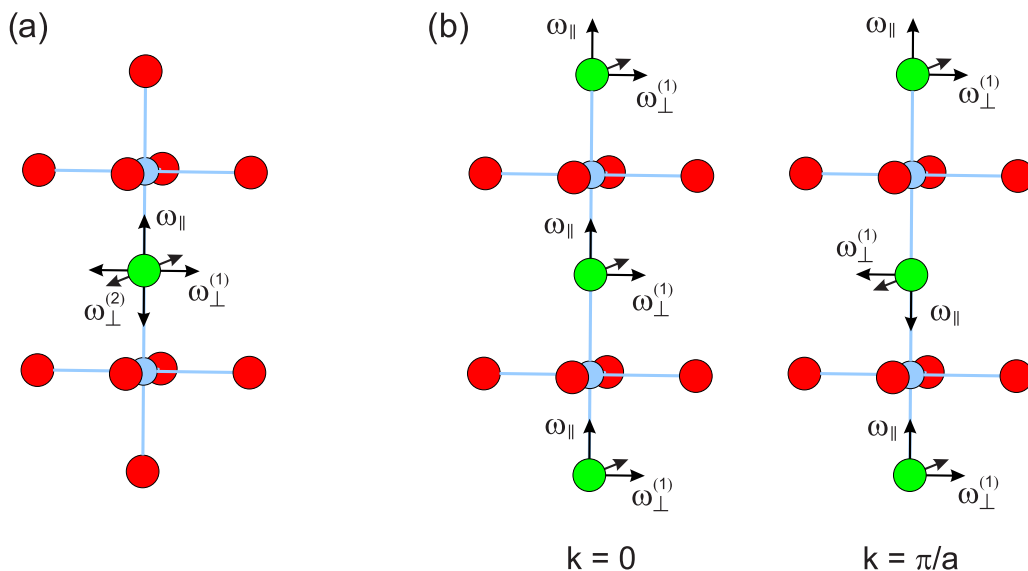


FIG. 2. Illustration of the oscillatorlike vibrational H modes in BaTiO<sub>3–x</sub>H<sub>x</sub> (a) and dispersed modes in SrVO<sub>2</sub>H (b). Ti/V, O, H atoms are depicted as light blue, red, and green circles, respectively.

method described by Rey *et al.* [13], was thoroughly mixed with 1.6 molar equivalents of H of CaH<sub>2</sub> (0.9 g, Sigma Aldrich, 99.9% purity) in an Ar-filled glove box. The mixture was pressed into pellets of 8 mm diameter, which were stacked and sealed inside a stainless-steel autoclave. The autoclave was then transferred outside the glove box, pressurized with 20 bar H<sub>2</sub> and heated in a vertical tube furnace at 600 °C for two days. To obtain a single-phase tetragonal product, the procedure had to be repeated two times. This involved regrinding the pellets and the addition of extra CaH<sub>2</sub>. As a last step, the sample was thoroughly washed several times with batches of 50 ml of 0.1 M acetic acid (HAc) and then with pure water and ethanol. The so purified sample was dried at 120 °C under dynamic vacuum ( $<10^{-5}$  bar). The final amount of product was about 3 g. The phase purity of the sample was examined by powder x-ray diffraction (PXRD). Rietveld analysis of the PXRD data confirmed that the obtained product was essentially phase pure and corresponded to SrVO<sub>2</sub>H as originally reported by Romero *et al.* [2]. For details, see the Supplemental Material [14].

### B. Inelastic neutron scattering

INS spectra were measured on the direct-geometry time-of-flight spectrometer MAPS at the ISIS Neutron and Muon Source, U.K. [15]. A 2.8 g powder sample of SrVO<sub>2</sub>H was filled into a rectangular aluminum sample can, which was sealed by an In wire. INS spectra were measured at base temperature of 10 K, using four different incident neutron energies ( $E_i$ ) of 650 (600), 350 (400), 250 (400), and 150 (200) meV (Fermi chopper frequency (Hz) in brackets). Standard data reduction was performed within MANTID software [16].

Complementary INS measurements were performed at the disk chopper spectrometer (DCS) at the NIST Center for Neutron Research, U.S. [17]. A measurement was performed at 430 K using an incident neutron wavelength of 8 Å. The generalized phonon density of states (GDOS) were derived from the time-of-flight data on the neutron energy gain side within the incoherent approximation [18] using DAVE software [19].

### C. Infrared spectroscopy

IR spectroscopy measurements were performed in transmittance mode over the frequency range 50–4000 cm<sup>-1</sup> using a Bruker IFS 66v/s FTIR spectrometer. A Mylar-6 beam splitter was used for measuring in the frequency range 50–450 cm<sup>-1</sup> (far-IR) and a KBr beam splitter was used for measuring in the frequency range 400–4000 cm<sup>-1</sup> (mid-IR). Parts of the powder sample were homogeneously dispersed to around 2 wt % in 0.2 g KBr powder and to 8 wt % in 0.04 g polyethylene (PE) and pressed to pellets under a load of 8 tons. The KBr pellet was used for the mid-IR range and the PE pellet was used for the far-IR range. The spectra of pellets of pure KBr and PE were used as reference spectra for the mid-IR and far-IR measurements, respectively. Absorbance spectra were obtained by taking the logarithm of the ratio of reference and sample spectra. High-temperature (300–570 K) mid-IR spectra were recorded using a heating block attached

to the sample chamber module of the IR spectrometer. Low-temperature (80–300 K) mid-IR spectra were recorded using a liquid-nitrogen bath cryostat attached to the sample chamber module of the IR spectrometer.

### D. Density functional theory calculations

DFT calculations were performed within the Projector-Augmented Wave method [20] as implemented in the VIENNA AB INITIO SIMULATION PACKAGE (VASP) [21,22]. The Perdew-Burke-Erzenhof (PBE) approximation was chosen for the exchange and correlation potential and energy [23]. A  $2 \times 2 \times 2$  supercell [made of the ten-atom body-centered tetragonal (bct) unit cell of AFM SrVO<sub>2</sub>H, which corresponds to a  $\sqrt{2} \times \sqrt{2} \times 2$  expansion of the five-atom primitive unit cell [2], cf. Fig. 1(c)] was used for phonon calculations. The integration over the Brillouin zone was done on a  $2 \times 2 \times 2$  Monkhorst-Pack  $k$ -point grid [24] and using the Gaussian smearing scheme. Strong electron correlations attributed to the localized 3d orbitals of V were treated using the PBE +  $U$  approach according to the scheme of Dudarev *et al.* [25]. In all the PBE +  $U$  calculations, the effective  $U$  was set to 2 eV [26]. The dynamical matrix was obtained via density functional perturbation theory as implemented in VASP and calculated with the PHONOPY program [27]. A plane-wave energy cutoff of 800 eV (VASP) was used in all calculations. Two structures, one with the AFM arrangement of spins as well as the nonmagnetic (NM) case were considered. Both structures were relaxed to their equilibrium volume and shape. The NM structure based on the ten-atom AFM bct unit cell turned out to be dynamically unstable with respect to a slight distortion of the O sublattice. The relaxed AFM structure ( $a = 5.5156$  Å,  $c = 7.3728$  Å,  $c/a = 1.337$ ,  $\mu = 1.73 \mu_B$ ) compares very well with the experimental structure ( $a = 5.5522$  Å,  $c = 7.3138$  Å,  $c/a = 1.317$ ,  $V = 56.45$  Å<sup>3</sup>/f.u.,  $\mu = 1.56 \mu_B$ ) [2], thus justifying the choice of the computational approach and especially the choice of the  $U$  parameter. aCLIMAX was used to generate INS spectra from the DFT computed eigenvectors and displacements [28,29].

## III. RESULTS

### A. Inelastic neutron scattering

It is instructive to first provide a qualitative vibrational analysis of SrVO<sub>2</sub>H. The NM primitive tetragonal unit cell contains five atoms, giving rise to 15 normal modes of vibration (three acoustic and 12 optical ones). The optical modes at the  $\Gamma$  – point distribute as follows when arranged in order of decreasing energy: V–H stretch,  $A_{2u}$ ; V–H bend,  $E_u$ ; V–O in-plane ( $x, y$ ) stretch,  $E_u$ ; V–O in-plane ( $x, y$ ) bend,  $E_u$ ; V–O out-of-plane ( $z$ ) puckering,  $A_{2u}$ ; V–O out-of-plane ( $z$ ) bend,  $B_{2u}$ , and three Sr–O vibrations [ $E_u(x, y)$  and  $A_{2u}(z)$ ]. The modes involving V–O and V–H vibrations are illustrated in Fig. 3.

Figure 4 shows the INS spectrum of SrVO<sub>2</sub>H measured at  $T = 10$  K over a broad spectral range, as obtained from the MAPS spectrometer using different  $E_i$ . The spectrum is dominated by a split peak around  $\approx 800$  cm<sup>-1</sup>. This peak is assigned to V–H bending, in accordance with previous studies on BaTiO<sub>3-x</sub>H<sub>x</sub> [11,12] and, as we will show later,

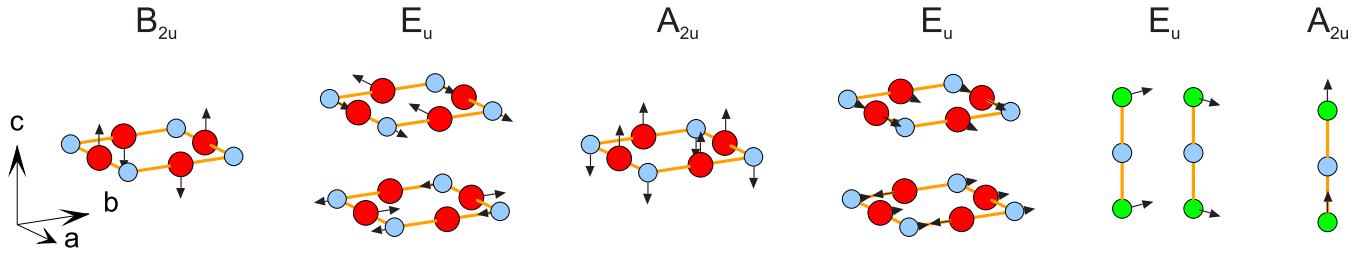


FIG. 3. Illustration of the optical modes involving V–O and V–H vibrations for the five-atom NM SrVO<sub>2</sub>H structure. V, O, H atoms are depicted as light blue, red, and green circles, respectively.

the split arises from the doubling of the unit cell because of the AFM structure. The broader peaks at  $\approx 1700\text{ cm}^{-1}$ ,  $\approx 2500\text{ cm}^{-1}$ ,  $\approx 3400\text{ cm}^{-1}$ , and  $\approx 4250\text{ cm}^{-1}$  are then overtones resulting from transitions to higher order states. The intensity at  $1050\text{ cm}^{-1}$  is attributed to a phonon wing, i.e. a combination band formed from the V–H bending mode and low-energy Sr–O lattice modes. A distinct V–H stretching mode is not clearly visible, which may be due to a large phonon dispersion that leads to a more complex line shape in the vibrational density of states (vDOS). At the same time, we recognize the complex shape of scattered intensity in the region  $1400\text{--}1900\text{ cm}^{-1}$ , which possibly contains a contribution from the V–H stretching mode, and provide a detailed analysis later. Scattered intensity in the low-energy region (up to  $600\text{ cm}^{-1}$ ) is contaminated with a contribution from the Al sample container at  $\approx 150$  and  $\approx 290\text{ cm}^{-1}$  (marked in Fig. 4). The broad peak at  $200\text{ cm}^{-1}$  is attributed to Sr–O lattice modes, and the  $450$  and  $550\text{ cm}^{-1}$  peaks to V–O vibrations. The inset in Fig. 4 shows the GDOS at  $T = 430\text{ K}$ , as obtained from an INS measurement at the DCS instrument. This spectrum was background subtracted and thus provides a high-quality spectrum of the low-energy region. The GDOS suggests a quadratic Debye increase from acoustic phonons up until the first peak around  $125\text{ cm}^{-1}$ . This peak is most likely the first Van Hove singularity, which occurs at acoustic phonon energies at the Brillouin zone boundary. In addition, the lowest energy optical phonon at the  $\Gamma$  point is most likely

close in energy and would also give a peak in the GDOS. These low-energy modes mainly involve displacements of the Sr atoms. At higher energies, there are several optical phonon peaks which mainly involve Sr–O and V–O vibrations, as marked in Fig. 4.

The momentum transfer ( $q$ ) dependence of the INS spectrum is illustrated in Fig. 5, which shows the  $S(q, E)$  map as measured using an incident neutron energy of  $350\text{ meV}$ , together with the spectra integrated over low  $q$  ( $0 < q < 8\text{ \AA}^{-1}$ ) and high  $q$  ( $8 < q < 12\text{ \AA}^{-1}$ ), respectively. All peaks showed an increasing intensity with increasing  $q$ , thus indicating that they correspond to phonon peaks, and we do not find evidence of magnetic excitations in the  $(q, E)$  range as probed here. However, at the same time we cannot exclude (AFM) spin wave excitations, since our data did not allow reliable analysis of scattered intensity in the low-energy region. For a complete compilation of  $S(q, E)$  maps, we refer to the supplemental material, Fig. S2.

The intensity of a vibrational band with energy  $E$  in INS is for a powder sample, within the incoherent approximation, proportional to the simplified expression [30]:

$$S(q, nE) \propto \frac{(q u_i)^{2n} \sigma_{\text{inc}} \exp[-(qU_{\text{tot}})^2]}{n!}, \quad (1)$$

where  $n$  is the order of the vibrational transition ( $n = 1$  for fundamentals,  $n = 2, 3, \dots$  for overtones and combination bands),  $u_i^2$  is the isotropic mean square displacement of the considered vibration,  $U_{\text{tot}}^2$  is the total isotropic mean square displacement, and  $\sigma_{\text{inc}}$  is the incoherent neutron scattering cross section. It follows that the INS intensity increases as  $q^{2n}$  ( $q^2$  for fundamentals) for low  $q$  and then becomes damped by the Debye-Waller factor at higher  $q$ , with a maximum occurring at  $q = \sqrt{(n/U_{\text{tot}}^2)}$ . This means that for overtones and combination bands, the intensity maximum will occur for higher  $q$  values.

By inspecting the  $S(q, E)$  map in Fig. 5(a), it is clear that the intensity of the complex-shaped peak between  $1400$  and  $1900\text{ cm}^{-1}$  has a maximum occurring at higher  $q$  than the H–V bend vibration around  $800\text{ cm}^{-1}$ . This is consistent with the assumption that the main intensity between  $1400$  and  $1900\text{ cm}^{-1}$  comes from overtones and a combination band of the split H–V bend peak. However, inspecting the spectra integrated over the low- $q$  and high- $q$  regions, respectively [Fig. 5(b)], we see that for the low- $q$  spectrum, the small shoulder peaks at  $1530\text{ cm}^{-1}$  and  $1790\text{ cm}^{-1}$  are more pronounced and that their relative intensity to the main peak at  $1680\text{ cm}^{-1}$  is larger. This indicates that the shoulder peaks at  $1530\text{ cm}^{-1}$  and  $1790\text{ cm}^{-1}$  originate from fundamental

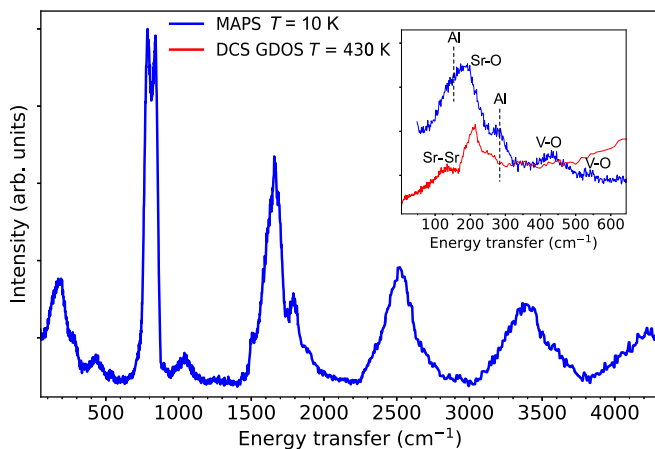


FIG. 4. INS spectrum of SrVO<sub>2</sub>H as measured on MAPS at  $10\text{ K}$ . The spectrum is a compilation of spectra measured with different incident neutron energies. The inset shows a zoom of the low-energy region together with tentative assignments of the peaks.

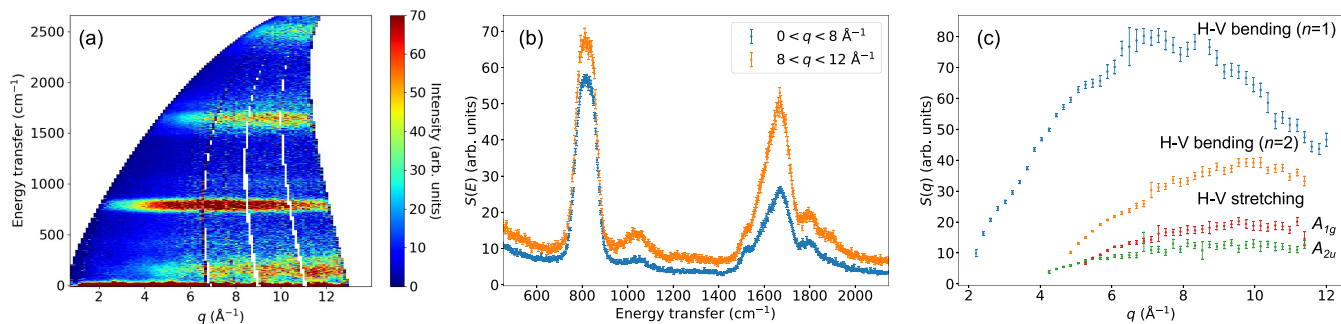


FIG. 5. (a)  $S(q, E)$  intensity map of SrVO<sub>2</sub>H as measured on MAPS using an incident neutron energy of 350 meV. (b) The spectra in (a) integrated over high and low  $q$  regions, respectively. Note that the energy resolution is not sufficient to resolve the split of the H–V bending mode around 800 cm<sup>-1</sup>. (c)  $S(q)$  integrated over the different energy regions corresponding to H–V bending mode (769–875 cm<sup>-1</sup>), H–V bending overtone (1553–1737 cm<sup>-1</sup>), and over the smaller shoulder peaks between 1463 and 1535 cm<sup>-1</sup> and between 1746 and 1835 cm<sup>-1</sup>, which we assign to stretching mode components. Note that the integrated intensity of these latter shoulder peaks also overlaps slightly with the main overtone intensity, and the higher energy shoulder overlaps in addition with a phonon wing peak around 1900 cm<sup>-1</sup>.

transitions and we tentatively assign them to the V–H stretch vibration, which, similarly to the V–H bending mode, is expected to be split due to the AFM structure.

### B. Infrared spectroscopy

Figure 6 shows the IR absorbance spectrum of SrVO<sub>2</sub>H, with the INS spectrum overlaid. The IR absorbance spectrum reveals three main bands within the frequency range of 400–4000 cm<sup>-1</sup>; a broad band between 500 and 700 cm<sup>-1</sup>, with a maximum at 580 cm<sup>-1</sup>, a sharp band at 840 cm<sup>-1</sup>, and a broad band between 1000 and 1650 cm<sup>-1</sup>, with a maximum at around 1500 cm<sup>-1</sup>. In addition, the presence of a sharp band is hinted at ≈ 420 cm<sup>-1</sup>. The lowest energy bands are assigned to V–O vibrations. The sharp 840 cm<sup>-1</sup> band coincides with the higher energy part of the split peak in the INS spectrum and is thus assigned to the V–H–V bending mode. The broad band between 1000 and 1650 cm<sup>-1</sup> is assigned to V–H stretching motions. Note that its maximum roughly coincides with the low-energy shoulder of the complex shaped INS band in the 1400–1900 cm<sup>-1</sup> range, thus strengthening the assignment of this intensity to the H–V stretch component in the INS spectrum. The slight differences in frequency of the bands in the IR

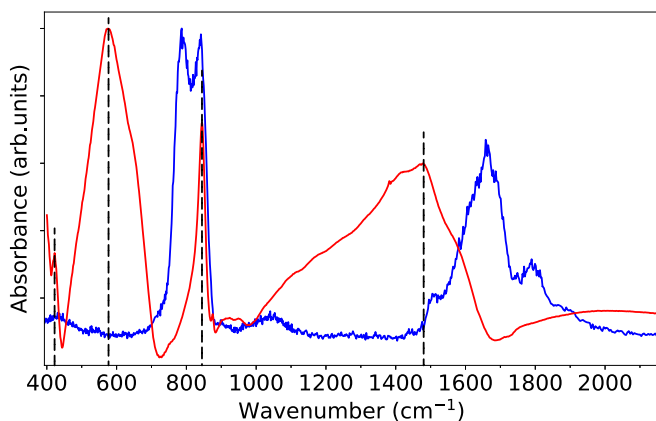


FIG. 6. Background subtracted mid-IR spectrum measured at room temperature (red line) compared to the INS spectrum measured on MAPS (blue line). The dashed lines mark the peak intensity of the four main bands in the IR spectrum.

and INS spectra can be related to the different measurement temperatures and the different parts of phonon wave vectors that are probed (IR spectroscopy only probes phonons at the  $\Gamma$  point). We also note the complex and broad line shapes of the V–O and H–V stretching modes. The broad nature of these bands is at present unclear, but we speculate that it is an effect of electrical anharmonicity, and hence different IR activity, in different local structural environments, in addition to just inhomogeneous band broadening because of different vibrational frequency in different local structures.

The far-IR spectrum is shown as Supplemental Material Fig. S3, and reveals an additional sharp peak at around 185 cm<sup>-1</sup>. This peak is most likely related to a Sr–O mode and is also in agreement with the lowest energy peak in the INS spectrum. The far-IR spectrum also reveals smaller peaks at around 310 cm<sup>-1</sup>, 355 cm<sup>-1</sup>, and 420 cm<sup>-1</sup>, the latter one which is also seen in the mid-IR spectrum in Fig. 6. These peaks are assigned to V–O modes.

### C. Density functional theory calculations

We first considered computing phonons for NM SrVO<sub>2</sub>H to obtain an overall impression of the vibrational properties for this compound (cf. Fig. 3). However, we found that the simple five-atom unit cell structure is not dynamically stable but displays imaginary phonons. The analysis of these phonons suggested a distortion of the O substructure in the tetragonal plane which can be expressed as minute clock- and counterclockwise rotations of every other square in the planar 4<sup>4</sup> net, which is shown as Supplemental Material Fig. S6. This results in a body-centered tetragonal cell, with  $a' = \sqrt{2}a$  and  $c' = 2c$  (space group symmetry  $I4/mcm$ ), that is analogous to the AFM cell (the corresponding primitive cell has a double size (10 atoms) with respect to the simple five-atom structure). The distorted structure is by 0.153 eV/f.u. more stable than the dynamically unstable five-atom structure. Taking AFM into account stabilizes SrVO<sub>2</sub>H additionally by 0.741 eV/f.u. The equilibrium volume is 56.07 Å<sup>3</sup>/f.u. and 57.60 Å<sup>3</sup>/f.u. for the AFM and NM structures, respectively. The (ten-atom) dynamically stable NM and AFM structures ( $D_{4h}$ ) give rise to 27 optical modes of which 14 are IR and 11 Raman active (and two inactive). These distribute over six V–H modes, 12

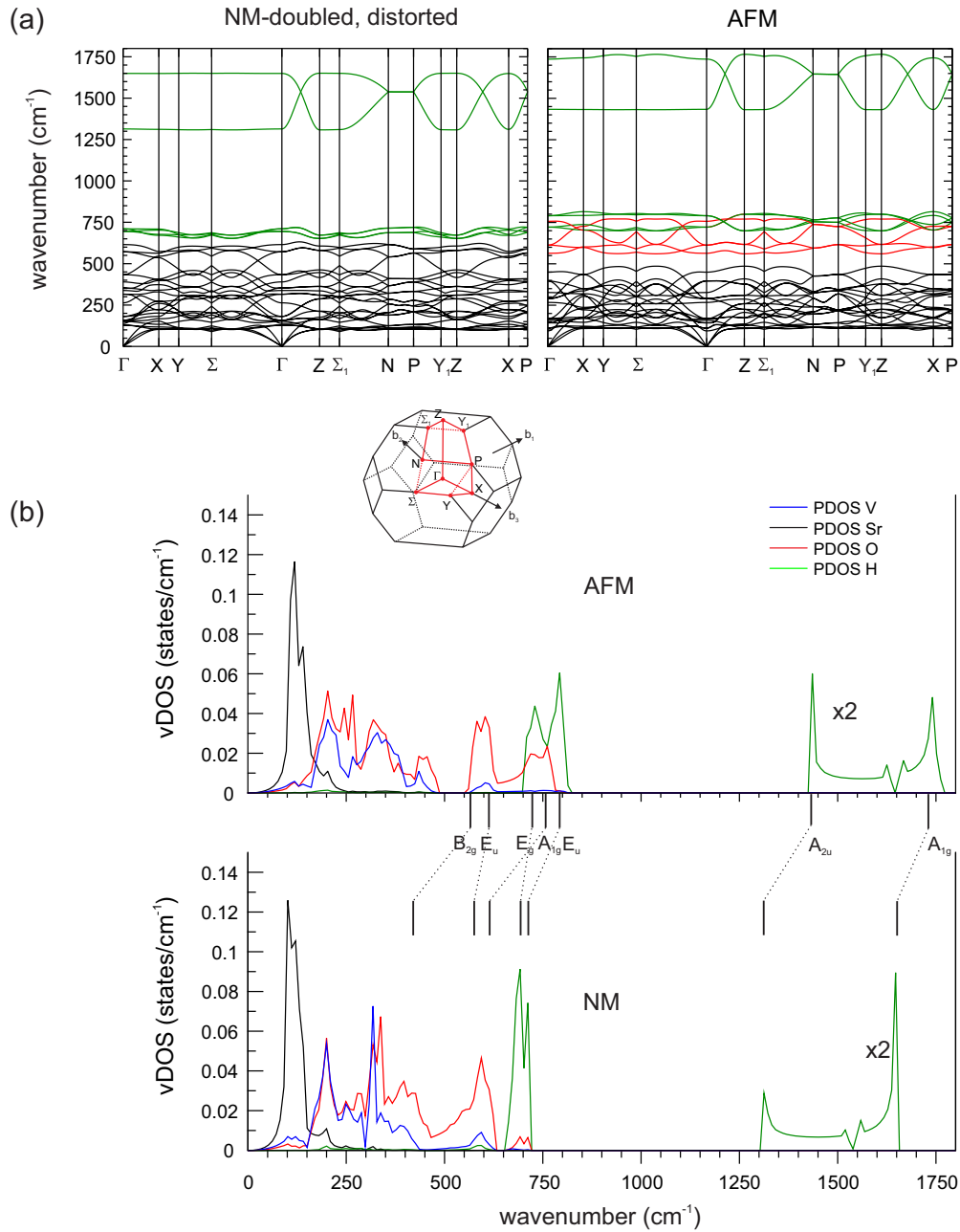


FIG. 7. Calculated phonon dispersions for the SrVO<sub>2</sub>H NM-10 atom (left) and AFM structure (right). H-based modes are highlighted in green and V-O in-plane modes are highlighted in red for the AFM structure where they are separated from the V-O out-of-plane modes. (b) Vibrational density of states (vDOS) for the SrVO<sub>2</sub>H NM-10 atom (lower panel) and AFM (upper panel) structures, decomposed into atomic contributions. (Note that the H-vDOS in the region 1000–1750 cm<sup>-1</sup> is scaled by a factor of 2). The location of H<sup>-</sup> and V-O in-plane modes at  $\Gamma$  are indicated by vertical line.

V-O modes, six Sr-O and 3 Sr-Sr modes. For simplicity we keep the classification of modes according to Fig. 3 also for the double cell structures. For the double cell structure, the V-H stretching mode splits into a  $A_{2u}$  and  $A_{1g}$  component (of which  $A_{2u}$  is observed in IR) and the V-H bending mode splits into a  $E_u$  and a  $E_g$  component (of which  $E_u$  is observed in IR). The V-O in plane ( $x, y$ ) stretching modes split into  $A_{1g}$ ,  $E_u$  and  $B_{2g}$  components.

Figure 7 compares the calculated phonon dispersion for the ten-atom SrVO<sub>2</sub>H NM and AFM structures [Fig. 7(a)] and the corresponding vDOS [Fig. 7(b)]. As expected, we find the V-

H stretching modes highest in energy (the IR active  $A_{2u}$  mode is at around 1250 cm<sup>-1</sup>) and highly dispersed along directions containing a  $z^*$  contribution. In particular, the dispersion along  $\Gamma - Z$  is larger than 300 cm<sup>-1</sup>. In contrast, the degenerate V-H bending modes are virtually dispersionless and localized at around 750 cm<sup>-1</sup>. It is now clear that the split feature of the bending mode in the INS spectrum is a consequence of the unit cell doubling. The IR active  $E_u$  component is at higher wave numbers. The four V-O in-plane stretching modes adjoin to the V-H bending modes and are located in the region down to 500 cm<sup>-1</sup>. There are noticeable differences between

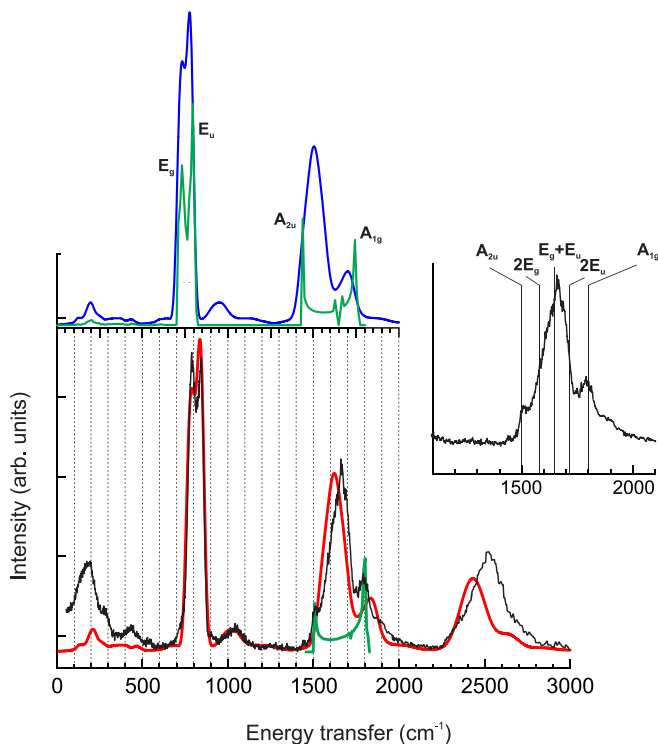


FIG. 8. Comparison of the measured (black line) and aClimax-simulated (red line) INS spectrum of SrVO<sub>2</sub>H. The simulated spectrum is scaled by 8% to match the experimental spectrum in the region of the V–H bending modes (700–900 cm<sup>-1</sup>). The upper part of the figure shows the aClimax simulated spectrum without scaling (blue line), together with the computed vDOS for H (green line). The green curve inset in the experimental spectrum suggests the real shape of the H–vDOS for the V–H stretching mode (with a dispersion over 300 cm<sup>-1</sup> and starting at 1500 cm<sup>-1</sup>). The discrepancy between simulated and experimental spectra in the ranges 1800–2000 and 2600–3000 cm<sup>-1</sup> is attributed to the slight mismatch of the H–vDOS for the V–H stretching mode. The upper right inset emphasizes the 1400–1900 cm<sup>-1</sup> region where bending mode overtones and stretching modes overlap. Their approximate locations at  $\Gamma$  are indicated.

the phonon dispersions of the NM and AFM structures. This is partly because of the slight structural distortion of the NM structure, but we infer that the differences are largely a consequence of AFM. The magnetic order of SrVO<sub>2</sub>H causes a pronounced stiffening of the V–H stretching modes and also a significant stiffening of the V–H bending modes along with an increase of the  $E_g - E_u$  split feature. Also the energies and order of the V–O modes are largely influenced by the AFM, whereas modes involving Sr ions appear essentially unaffected [Fig. 7(b)].

The coupling of spins to optical phonons is a well-known phenomenon and has been investigated earlier for perovskite and spinel-like materials [31–37]. In the conventional formulation of the spin-phonon coupling effect, coupling occurs if the exchange integrals are sensitive to a normal coordinate, leading to magnetic contributions to the harmonic energy of the lattice [38]. Typically, frequency shifts are in a range of several cm<sup>-1</sup> to several tens of cm<sup>-1</sup> [39]. A record high frequency shift of 40 cm<sup>-1</sup> has been recently reported for

NaOsO<sub>3</sub> [40]. It appears that frequency shifts are larger for SrVO<sub>2</sub>H, possibly exceeding 100 cm<sup>-1</sup> for both V–H and V–O-based modes.

We conjecture that magnetism couples to phonons in SrVO<sub>2</sub>H on an unprecedented scale and the reason for this should originate from the changes in hybridization due to spin ordering as described in Ref. [39]. We notice that the spin exchange parameters within the V–O plane are large (23.54 meV [10] / 42.7 meV [9]), so one would expect sizable spin-phonon coupling for the V–O-based modes. However, the interlayer exchange is an order of magnitude smaller, yet V–H-based phonons are strongly influenced by spin-phonon coupling. This may be attributed to the large displacement of H resulting in substantial stiffening of the corresponding force constants and, thus, one could generally expect large spin-phonon coupling effects for magnetic hydrides. In principle, quantification of these effects could be done within a general approach suggested in Ref. [32], which incorporates material-specific information from first principles into spin-phonon coupling models.

We now turn to a comparison of the DFT-computed vibrational frequencies with the INS spectrum of SrVO<sub>2</sub>H. This is shown in Fig. 8. For most parts, the computed frequencies are underestimated. However, when scaling their frequency by 8%, the V–H bending modes fall in the same range as in the experimental INS spectrum. The aClimax-simulated spectrum based on the scaled energies reproduces the experimental intensity of the bending modes very well. This implies that also the contribution of their overtones ( $2 \times 790$  cm<sup>-1</sup>,  $2 \times 840$  cm<sup>-1</sup>) and combination ( $790 + 840$  cm<sup>-1</sup>) to the complex scattering intensity between 1400 and 1900 cm<sup>-1</sup> should be properly described (provided that anharmonicity is negligible). Deviations of the aClimax-simulated spectrum in this region can then be attributed to a slightly erroneously calculated V–H stretching mode, which is estimated to disperse from 1500 to 1800 cm<sup>-1</sup> instead of from 1550 to 1875 cm<sup>-1</sup> (after scaling). The inset in Fig. 8 illustrates the scattering intensity in the region 1400–1900 cm<sup>-1</sup> as a superposition of stretching mode components and bending mode overtones/combination.

#### IV. DISCUSSION

The vibrational properties of SrVO<sub>2</sub>H are distinguished by the narrowly and widely dispersed V–H bending and stretching modes, respectively. The analysis of its INS spectrum is somewhat obstructed by the overlap of the bending overtones with the stretching fundamental. We compare our results on SrVO<sub>2</sub>H with previous INS studies on BaTiO<sub>3-x</sub>H<sub>x</sub> possessing an average cubic perovskite structure. Because of the low concentration ( $x = 0.1 - 0.2$ ) and disorder of H, H-based vibrations in BaTiO<sub>3-x</sub>H<sub>x</sub> rather correspond to localized oscillators than dispersed phonons [11,12]. The location of the bending vibration of BaTiO<sub>3-x</sub>H<sub>x</sub> (at 900 cm<sup>-1</sup>) is somewhat higher than the corresponding mode in SrVO<sub>2</sub>H. Upon bending, the H ions displace toward the alkaline earth metal (A) ions in the tetragonal plane. We note that the interatomic distances Sr–H and Ba–H are 2.78 and 2.83 Å, respectively, which does not reflect the difference in the ionic radii of Sr<sup>2+</sup> (1.13 Å) and Ba<sup>2+</sup> (1.35 Å)—i.e., from the sum of ionic radii a

smaller (larger) distance would be expected for Sr–H (Ba–H). This could indicate weaker A–H interactions in SrVO<sub>2</sub>H and thus explain the somewhat lower frequency of its bending mode. By contrast, if assigning the center of the stretching band to an oscillator frequency, it is about 1450 cm<sup>-1</sup> and 1600 cm<sup>-1</sup> for NM and AFM SrVO<sub>2</sub>H, respectively. This is considerably higher than for BaTiO<sub>3-x</sub>H<sub>x</sub> (1030 cm<sup>-1</sup>) and suggests considerably stronger V–H bonding interactions. This observation is in agreement with the theoretical work of Liu *et al.*, finding increased T–H bond strength when going from V to Fe due to the increased electronegativity of T [10].

We further concluded that the optical phonons of SrVO<sub>2</sub>H are largely influenced by spin-phonon coupling. At the same time, there is no direct experimental proof of this since it was not possible to measure spectra through the magnetic phase transition. The Néel temperature of SrVO<sub>2</sub>H is extraordinarily high, most likely above or around 600 K, and probably coinciding with the decomposition of the material. Large spin-phonon coupling was deduced from DFT calculations by comparing AFM SrVO<sub>2</sub>H with a NM reference structure. However, this comparison is somewhat hampered because hypothetical NM SrVO<sub>2</sub>H at zero Kelvin adopts a slightly distorted structure. Interestingly, there are further representatives of strontium vanadium oxyhydrides, namely, the structurally related Ruddlesden-Popper phases Sr<sub>2</sub>VO<sub>3</sub>H and Sr<sub>3</sub>V<sub>2</sub>O<sub>5</sub>H<sub>2</sub> [2], which may allow experimental characterization of spin-phonon coupling and thus consolidation of this phenomenon in magnetic hydrides. As SrVO<sub>2</sub>H, these materials are also AFM but the Néel temperatures are considerably lower, ≈ 170 and ≈ 240 K, for Sr<sub>2</sub>VO<sub>3</sub>H and Sr<sub>3</sub>V<sub>2</sub>O<sub>5</sub>H<sub>2</sub>, respectively [2]. Spectroscopic studies, including INS, could thus be performed in a temperature range far below the decomposition temperature.

## V. CONCLUSIONS

The vibrational properties of the AFM oxyhydride SrVO<sub>2</sub>H have been studied by using a combination of INS, IR absorbance spectroscopy, and DFT calculations. Combined analyses of the experimental and theoretical data showed that the H-based vibrational modes are divided into a degenerate V–H bending mode centered around 800 cm<sup>-1</sup> and

a highly dispersed V–H stretching mode in the range 1500–1800 cm<sup>-1</sup>. Phonon calculations revealed a large coupling between magnetism and optical phonons in SrVO<sub>2</sub>H. This is prominently featured by a 50 cm<sup>-1</sup> split of the V–H bending vibrational mode into two components and frequency shifts of the H-based modes by 50–100 cm<sup>-1</sup>. Frequency shifts of the same order of magnitude occur also for V–O modes, which are located in the range 300–700 cm<sup>-1</sup>. The extent of spin-phonon coupling for V–H based modes appears surprising because the superexchange interaction via H is comparatively small. In conclusion, our study suggests that magnetic hydrides are an interesting playground for fundamental studies of spin-phonon coupling in materials. As a starting point for future exploration, the related Ruddlesden-Popper phases Sr<sub>2</sub>VO<sub>3</sub>H, and Sr<sub>3</sub>V<sub>2</sub>O<sub>5</sub>H<sub>2</sub> with Néel temperatures below room temperature represent attractive targets.

## ACKNOWLEDGMENTS

Ezio Zanghellini is thanked for assistance in the collection of the IR spectra. Mikael S. Andersson and Madhusudan Tyagi are acknowledged for their help in the data collection at NIST center for neutron research. This research was funded by the Swedish Research Council (Grants No. 2014-03980, No. 2016-06958, and No. 2019-05366). Also, support from the Swedish Foundation of Strategic Research (SSF) within the Swedish national graduate school in neutron scattering (SwedNess), Swedish Foundation for International Co-operation in Research and Higher Education (STINT), and the Brazilian Agency CAPES (Project No. CAPES/STINT N 88887.304724/2018) is acknowledged. Density functional calculations were performed on resources provided by the Swedish National Infrastructure for Computing (SNIC) at the National Supercomputer Centre (NSC). Experiments at the ISIS Neutron and Muon Source were supported by beamtime allocations from the Science and Technology Facilities Council. We acknowledge the support of the National Institute of Standards and Technology, U.S. Department of Commerce, in providing, in part, the neutron research facilities used in this paper.

- 
- [1] Y. Kobayashi, O. Hernandez, C. Tassel, and H. Kageyama, *Sci. Technol. Adv. Mater.* **18**, 905 (2017).
  - [2] F. Denis Romero, A. Leach, J. S. Möller, F. Foronda, S. J. Blundell, and M. A. Hayward, *Angew. Chem., Int. Ed.* **53**, 7556 (2014).
  - [3] C. Tassel, Y. Goto, Y. Kuno, J. Hester, M. Green, Y. Kobayashi, and H. Kageyama, *Angew. Chem., Int. Ed.* **53**, 10377 (2014).
  - [4] Y. Kobayashi, O. J. Hernandez, T. Sakaguchi, T. Yajima, T. Roisnel, Y. Tsujimoto, M. Morita, Y. Noda, Y. Mogami, A. Kitada, M. Ohkura, S. Hosokawa, Z. Li, K. Hayashi, Y. Kusano, J. E. Kim, N. Tsuji, A. Fujiwara, Y. Matsushita, K. Yoshimura *et al.*, *Nat. Mater.* **11**, 507 (2012).
  - [5] T. Yajima, A. Kitada, Y. Kobayashi, T. Sakaguchi, G. Bouilly, S. Kasahara, T. Terashima, M. Takano, and H. Kageyama, *J. Am. Chem. Soc.* **134**, 8782 (2012).
  - [6] R. Lavén, U. Häussermann, A. Perrichon, M. S. Andersson, M. S. Targama, F. Demmel, and M. Karlsson, *Chem. Mater.* **33**, 2967 (2021).
  - [7] N. Masuda, Y. Kobayashi, O. Hernandez, T. Bataille, S. Paofai, H. Suzuki, C. Ritter, N. Ichijo, Y. Noda, K. Takegoshi, C. Tassel, T. Yamamoto, and H. Kageyama, *J. Am. Chem. Soc.* **137**, 15315 (2015).
  - [8] T. Yajima, F. Takeiri, K. Aidzu, H. Akamatsu, K. Fujita, W. Yoshimune, M. Ohkura, S. Lei, V. Gopalan, K. Tanaka, C. M. Brown, M. A. Green, T. Yamamoto, Y. Kobayashi, and H. Kageyama, *Nat. Chem.* **7**, 1017 (2015).
  - [9] Y. Wei, H. Gui, X. Li, Z. Zhao, Y. H. Zhao, and W. Xie, *J. Phys.: Condens. Matter* **27**, 206001 (2015).
  - [10] K. Liu, Y. Hou, X. Gong, and H. Xiang, *Sci. Rep.* **6**, 19653 (2016).



- [11] E. J. Granhed, A. Lindman, C. Eklöf-Österberg, M. Karlsson, S. F. Parker, and G. Wahnström, *J. Mater. Chem. A* **7**, 16211 (2019).
- [12] C. Eklöf-Österberg, L. Mazzei, E. J. Granhed, G. Wahnström, R. Nedumkandathil, U. Häussermann, A. Jaworski, A. J. Pell, S. F. Parker, N. H. Jalarvo, L. Börjesson, and M. Karlsson, *J. Mater. Chem. A* **8**, 6360 (2020).
- [13] M. J. Rey, J. C. Joubert, B. Lambert Andron, M. Cyrot, and F. Cyrot-Lackmann, *J. Solid State Chem.* **86**, 101 (1990).
- [14] See Supplemental Material at <http://link.aps.org/supplemental/10.1103/PhysRevMaterials.6.024409> for additional powder x-ray characterization, additional INS, IR, and DFT data, DFT optimized structures, and which contains Refs. [41–43].
- [15] R. A. Ewings, J. R. Stewart, T. G. Perring, R. I. Bewley, M. D. Le, D. Raspino, D. E. Pooley, G. Škoro, S. P. Waller, D. Zacek, C. A. Smith, and R. C. Riehl-Shaw, *Rev. Sci. Instrum.* **90**, 035110 (2019).
- [16] O. Arnold, J. C. Bilheux, J. M. Borreguero, A. Buts, S. I. Campbell, L. Chapon, M. Doucet, N. Draper, R. Ferraz Leal, M. A. Gigg, V. E. Lynch, A. Markvardsen, D. J. Mikkelsen, R. L. Mikkelsen, R. Miller, K. Palmen, P. Parker, G. Passos, T. G. Perring, P. F. Peterson *et al.*, *Nucl. Instrum. Methods Phys. Res., Sec. A* **764**, 156 (2014).
- [17] J. R. D. Copley and J. C. Cook, *Chem. Phys.* **292**, 477 (2003).
- [18] B. Chazallon, H. Itoh, M. Koza, W. F. Kuhs, and H. Schober, *Phys. Chem. Chem. Phys.* **4**, 4809 (2002).
- [19] R. T. Azuah, L. R. Kneller, Y. Qiu, P. L. Tregenna-Piggott, C. M. Brown, J. R. Copley, and R. M. Dimeo, *J. Res. Natl. Inst. Stand. Technol.* **114**, 341 (2009).
- [20] P. E. Blöchl, *Phys. Rev. B* **50**, 17953 (1994).
- [21] G. Kresse and J. Hafner, *Phys. Rev. B* **47**, 558 (1993).
- [22] G. Kresse and J. Furthmüller, *Phys. Rev. B* **54**, 11169 (1996).
- [23] J. P. Perdew, K. Burke, and M. Ernzerhof, *Phys. Rev. Lett.* **77**, 3865 (1996).
- [24] H. J. Monkhorst and J. D. Pack, *Phys. Rev. B* **13**, 5188 (1976).
- [25] S. L. Dudarev, G. A. Botton, S. Y. Savrasov, C. J. Humphreys, and A. P. Sutton, *Phys. Rev. B* **57**, 1505 (1998).
- [26] T. Yamamoto, D. Zeng, T. Kawakami, V. Arcisauskaite, K. Yata, M. A. Patino, N. Izumo, J. E. McGrady, H. Kageyama, and M. A. Hayward, *Nat. Commun.* **8**, 1217 (2017).
- [27] A. Togo and I. Tanaka, *Scr. Mater.* **108**, 1 (2015).
- [28] D. Champion, J. Tomkinson, and G. Kearley, *Appl. Phys. A* **74**, s1302 (2002).
- [29] A. Ramirez-Cuesta, *Comput. Phys. Commun.* **157**, 226 (2004).
- [30] P. C. H. Mitchell, S. F. Parker, A. J. Ramirez-Cueza, and J. Tomkinson, *Vibrational Spectroscopy with Neutrons* (World Scientific, Singapore, 2005).
- [31] A. F. García-Flores, A. F. L. Moreira, U. F. Kaneko, F. M. Ardito, H. Terashita, M. T. D. Orlando, J. Gopalakrishnan, K. Ramesha, and E. Granado, *Phys. Rev. Lett.* **108**, 177202 (2012).
- [32] C. J. Fennie and K. M. Rabe, *Phys. Rev. Lett.* **96**, 205505 (2006).
- [33] J. H. Lee and K. M. Rabe, *Phys. Rev. B* **84**, 104440 (2011).
- [34] C. Kant, M. Schmidt, Z. Wang, F. Mayr, V. Tsurkan, J. Deisenhofer, and A. Loidl, *Phys. Rev. Lett.* **108**, 177203 (2012).
- [35] S. Massidda, M. Posternak, A. Baldereschi, and R. Resta, *Phys. Rev. Lett.* **82**, 430 (1999).
- [36] T. Birol, N. A. Benedek, and C. J. Fennie, *Phys. Rev. Lett.* **107**, 257602 (2011).
- [37] Y. Zhou and K. M. Rabe, *Phys. Rev. B* **88**, 094416 (2013).
- [38] W. Baltensperger and J. S. Helman, *Helv. Phys. Acta* **41**, 668 (1968).
- [39] A. L. Wysocki and T. Birol, *Phys. Rev. B* **93**, 134425 (2016).
- [40] S. Calder, J. H. Lee, M. B. Stone, M. D. Lumsden, J. C. Lang, M. Feygenson, Z. Zhao, J. Q. Yan, Y. G. Shi, Y. S. Sun, Y. Tsujimoto, K. Yamaura, and A. D. Christianson, *Nat. Commun.* **6**, 8916 (2015).
- [41] J. Rodríguez-Carvajal, FULLPROF: A program for rietveld refinement and pattern matching analysis, *Abstracts of the Satellite Meeting on Powder Diffraction of the XV Congress of the IUCr, Toulouse, France* (Scientific Research Publishing Inc., 1990), p. 127.
- [42] P. Giannozzi, S. Baroni, N. Bonini, M. Calandra, R. Car, C. Cavazzoni, D. Ceresoli, G. L. Chiarotti, M. Cococcioni, I. Dabo, A. D. Corso, S. de Gironcoli, S. Fabris, G. Fratesi, R. Gebauer, U. Gerstmann, C. Gougoussis, A. Kokalj, M. Lazzeri, L. Martin-Samos *et al.*, *J. Phys.: Condens. Matter* **21**, 395502 (2009).
- [43] M. Methfessel and A. T. Paxton, *Phys. Rev. B* **40**, 3616 (1989).